Competition of quantum effects in H_2/D_2 sieving in narrow single-wall carbon nanotubes

Manel Mondelo-Martell[a,*] and Fermín Huarte-Larrañaga

Department of Materials Science and Physical Chemistry & Institute of Theoretical and Computational Chemistry, Faculty of Chemistry, Universitat de Barcelona, Barcelona, Spain

ARTICLE HISTORY
Compiled June 22, 2021

ABSTRACT
Nanoporous materials have the potential to be used as *molecular sieves* to separate chemical substances in a mixture via selective adsorption and kinetic sieving. The separation of isotopologues is also possible via the so-called *quantum sieving* effect: the different effective size of isotopologues due to their different Zero Point Energy (ZPE). Here we compare the diffusion coefficients of Hydrogen and Deuterium in (8,0) Single Walled Carbon Nanotubes obtained with quantum dynamics simulations. The diffusion channels obtained present important contributions from resonances connecting the potential wells. These resonances, which are more important for H_2 than for D_2, increase the low-temperature diffusivity of both isotopologues, but prevent the inverse kinetic isotope effect reported for similar nanostructured systems.

KEYWORDS
quantum confinement; quantum sieving; quantum dynamics

1. Introduction

The importance of hydrogen in chemical research and industry cannot be overestimated: from its use as reagent in synthetic chemistry and several industrial processes, to its potential application as a clean fuel for combustion batteries, the future of our society seems to be inevitably tied to being able to harness hydrogen's capabilities as efficiently as possible[1–3]. One particular aspect of such harnessing is the separation of hydrogen and deuterium, since the latter has very different applications in the areas of isotopological tracing[4], proton nuclear magnetic resonance spectroscopy[5, 6], neutron scattering[7, 8]. If chemical separation processes are extremely costly *per se*, using around 10-15% of the total amount of energy consumed worldwide[9], isotopological separation is comparatively the most expensive[10, 11]. In the particular case of H_2/D_2 separation, at industrial level the most common technique is the cryogenic distillation, which achieves a separation factor of merely 1.5[12]. Finding a more efficient pathway to achieve this separation is clearly one of the main objectives in current research in the area of chemical separation[3]. A very promising alternative is based on the *quantum*

---

[a] Current affiliation: Institute of Physical and Theoretical Chemistry, Goethe University Frankfurt, Frankfurt am Main, Germany

[*] Author to whom correspondence should be addressed: manel.mondelo@chemie.uni-frankfurt.de

sieving effect, proposed by Beenakker *et al*[13]. This phenomenon is a consequence the mass difference between H_2 and D_2: a lower mass increases the zero-point energy of the internuclear bond, which in turn results in a more diffuse wave function and therefore a larger *effective size*. Thus, H_2 has a larger effective size when compared with the heavier D_2. This size difference becomes critical when the molecules enter nanometric cavities, and can affect both their adsorption and diffusion properties. In the last two decades, the adsorption of H_2 and D_2 has been studied in several nanoporous materials such as carbon nanotubes[14–19], zeolites[20–23], or metal–organic frameworks (MOFs)[24–29] with the aim of finding the best candidate for isotopic separation of H_2 and D_2; see also Ref 30 and references therein. Very recently, specifically tailored organic cage molecules have been reported to obtain selectivities of up to 8 by combining small pores connecting large cavities[31].

When studying quantum sieving, one has to distinguish between the change of the adsorption and diffusion properties of the adsorbates. In the former case, a heavier isotopologue is preferentially adsorbed in the nanomaterial (*thermodynamic* or *chemical affinity* quantum sieving), which can be straightforwardly interpreted through the relative change in ZPE of the two species when entering the nanometric cavity. Regarding diffusion, it is known that there are two competing quantum effects which simultaneously play a role in the process: on one hand, the ZPE effects described above decrease the diffusion barrier for the heavier deuterium, resulting in a higher mobility than expected. This effect has been claimed to result in an *inverse kinetic isotope effect*, namely, a faster diffusion of deuterium in nanoporous materials, compared with hydrogen[32–34]. However, these studies were based on semiclassical Transition State Theory simulations, which neglect the second quantum effect: resonant tunnelling. A more detailed study of the diffusion of H_2/D_2 mixtures in broad (2.7 nm diamater) carbon nanotubes by Kowalczyk *et al.*[17] using Ring-polymer Molecular Dynamics showed the complex interplay of nuclear quantum effects in this process. However, for narrower carbon nanotubes (up to 0.6 nm diameter), which enforce single-file diffusion of the confined molecules, its has been seen that tunnelling effects contribute to enhance hydrogen transport properties[35].

In this work we revisit the case of H_2/D_2 quantum sieving in a narrow (8,0) single walled carbon nanotubes, with a diameter of 0.6 nm, and provide accurate diffusion coefficients for for both molecules in the low pressure regime. The results reported here evidence that by significantly extending the propagation time up to 20 picoseconds we are able to resolve quantum resonances below the diffusion barrier that change drastically the perspective of the previously published simulations. These much larger propagation times, required by the low corrugation of the potential energy profile along the nanotube axis, are achieved thanks to an adiabatic approach described in a previous work[35].

2. Theoretical Methods

2.1. Diffusion coefficient calculation

Previous theoretical works[33–37] on the diffusion of hydrogen in nanoporous carbon, regardless of the specific potential energy surface employed, show that the interaction between the molecule and the nanostructure generates a potential energy profile that consists of collection of minima (adsorption sites) separated by maxima (diffusion barriers). In the particular case of narrow carbon nanotubes as the (8,0) one studied here (0.6 nm diameter), the minima and maxima are located along the nanotube axis, and this structure forces single-file diffusion of the confined molecules. This limits the influence of interactions among adsorbed molecules, which will therefore be neglected hereafter. Given these features of the potential energy surface, and following previous studies[38] on similar systems, we have modelled the molecular diffusion process a set of uncorrelated jumps between neighbouring adsorptions sites separated by a distance l[39, 40]. Using this model and in the low-pressure limit the diffusion coefficient is obtained through:

$$D(T) = \frac{l^2}{2d} k_{hop}(T). \tag{1}$$

where k_{hop} is the hopping probability between adjacent sites, and d is the dimensionality of the system (1 in this case). The problem of calculating the diffusion coefficient is then reduced to the calculation of k_{hop}. Following Zhang and Light[38], this probability will be calculated through the flux–correlation function approach in a quantum dynamics formalism, which is summarised below.

The general expression for a transition rate $k(T)$ is given by the thermal average of the Cumulative Reaction Probability (CRP), $N(E)$, which defines the probability for the system to go from any reactant state to any product state as a function of the energy. Then, assuming a Boltzmann distribution for the energy of the system, we have:

$$k(T) = \frac{1}{2\pi Q(T)} \int_{-\infty}^{\infty} e^{-\beta E} N(E) dE. \tag{2}$$

In the previous equation, $\beta = \frac{1}{k_B T}$, and $Q(T)$ is the partition function of the system. In our case, the partition function of molecular hydrogen or deuterium is factorised as a product of its (5) confined degrees of freedom and the unconfined diffusion coordinate (z) (see below for details on the coordinate system used in the model):

$$Q(T) = \mathrm{Tr}(e^{\beta \hat{H}^{5D}}) q_z(T) \tag{3}$$

with $q_z(T) = L \left(\frac{mT}{2\pi}\right)^{\frac{1}{2}}$ the semiclassical partition function of a particle in a periodic potential with periodicity L equals to the unit cell's lenght (4 a_0 in our case) and $\hat{H}^{5D}$ the Hamiltonian of the *confined coordinates* of the system (see below). The origin of energy was chosen to be the minimum value of the PES (note that the origin of energy of both the partition function and $N(E)$ has to be chosen consistently to ensure that $k(T)$ does not depend on the energy reference taken).

In this work we compute $N(E)$ via the flux–correlation functions approach[41–43], as implemented in Refs 44, 45. In this approach one sets a dividing surface, h, which separates reactants from products and defines the thermal flux operator accross such a surface as $\hat{F}_{T_0} = e^{-\beta_0 \hat{H}/2} i[\hat{H}, h] e^{-\beta_0 \hat{H}/2} = e^{-\beta_0 \hat{H}/2} \hat{F} e^{-\beta_0 \hat{H}/2}$, with $\beta = 1/k_B T_0$. With this we can define the generalised flux-correlation function:

$$C_{ff}(t, t'; T_0) = \mathrm{Tr}(\hat{F}_{T_0} e^{i\hat{H}t'} \hat{F} e^{-i\hat{H}t}) \tag{4}$$

which is related to the Boltzmann averaged $N(E)$ through a Fourier transform:

$$N(E) = \frac{1}{2} e^{2\beta_0 E} \int_{-\infty}^{\infty} dt \int_{-\infty}^{\infty} dt' e^{\mathrm{i}E(t-t')} C_f(t,t';T_0). \tag{5}$$

In order to evaluate the trace in Eq (4) efficiently, the flux operator is diagonalised to obtain its eigenvalues and eigenstates (f_{T_0} and $|f_{T_0}\rangle$, respectively). It can be shown[46] that the flux operator has a limited spectrum of non-zero eigenvalues, and therefore the tracing operation can be performed over a comparatively small number of states. The flux correlation function is then computed from the time–propagated flux eigenstates as $C_{ff}(t) = \sum_{m,n} f_m f_n \langle f_n \mid e^{-\mathrm{i}\hat{H}t} \mid f_m \rangle$, and the final expression for the cumulative reaction probability becomes:

$$N(E) = \frac{1}{2} e^{2\beta_0 E} \sum_n \sum_m f_n f_m \left| \int_{-\infty}^{\infty} dt e^{\mathrm{i}Et} \langle f_n \mid e^{-\mathrm{i}\hat{H}t} \mid f_m \rangle \right|^2 . \tag{6}$$

Moreover, it can also be seen that the flux eigenstates of a system can be related to the vibrational states of the activated complex at the top of the dividing surface[47]. Therefore this method has the additional advantage that we can obtain the individual contributions of each flux eigenstate to the cumulative reaction probability, $N_i(E)$, so that the cumulative reaction probability is defined as the sum of this individual contributions [48]. This can give insight of the mechanism of the transition process.

In this work we have used the State-Averaged variant of the Multiconfigurational Time–dependent Hartree (SA-MCTDH)[45] for both the iterative diagonalisation of the different operators (Hamiltonian and flux operator), and the propagation of the resulting wavepackets.

2.2. Modelisation of the system

To represent the diffusion of H_2 (or D_2) in the low pressure limit and compute the transition rate in Eq. 2, we have modelled a single molecule in the hollow cavity of a carbon nanotube using its 3 internal degrees of freedom (vibration ρ, polar angle between molecular and nanotube axis θ, and azimuthal angle ϕ) as well as the 3 translational DOFs of the molecular centre of mass (x, y, z) as a coordinate system. This representation has been previously used by ourselves [35, 37, 49] as well as by other authors[15, 50]. The quantum dynamics calculations have been carried out using an adiabatic approximation described in a previous publication[35]. This is justified in terms of a time–scale separation argument between the large–amplitude motion of the molecule along the axis of the nanotube (z) and the fast motion on the *confined* coordinates (vibration, rotation, and translation in the xy plane; collectively referred to as q), as it can be inferred from the relaxed potential energy surfaces in Figure 1.

Following this approximation the full dynamics of the system is represented by the evolution of a 1D wavepacket on a set of particular potential energy surfaces instead of a full 6D function. The molecular wave packet evolves, thus, according to the 1D Time–dependent Schrödinger Equation (note that atomic units are used throughout this paper, and therefore $\hbar = 1$):

$$i\frac{\partial}{\partial t}\tilde{\psi}_j(z,t) = \hat{H}_j^{(ad)}\tilde{\psi}_j(z,t), \tag{7}$$

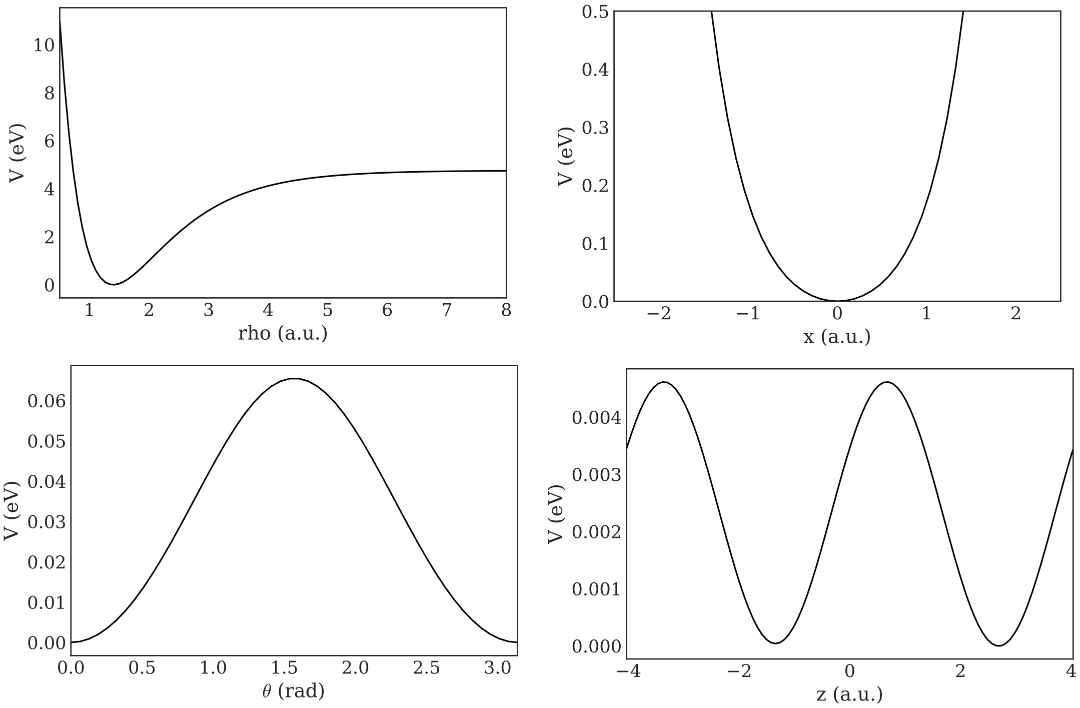

Figure 1. Relaxed projections of the PES used in this work along significant coordinates. Note the small corrugation along the z coordinate as compared to the potentials along ρ, θ and x.

with the adiabatic Hamiltonian defined as:

$$\hat{H}_j^{(ad)} = \frac{1}{2m}\frac{\partial^2}{\partial z^2}z + \sum_{k=1}^{N_z} \varepsilon_j(z_k)\,|z_k\rangle\langle z_k|\,, \tag{8}$$

with m the mass of H_2 or D_2, as needed.

In Eq (8), each function $\varepsilon_j(z_k)$ represents the z–dependent eigenvalue of a given eigenstate $\xi_j^{5D}(q;z_k)$ of the confined coordinates Hamiltonian, $\hat{H}^{5D}(q,z_k)$, evaluated at a given grid point z_k. By including the projector $|z_k\rangle\langle z_k|$ this function acts effectively as a potential energy term for the motion of the wave packet along the z dimension. We will hence refer to each $\varepsilon_j(z_k)$ as a *confined eigenstate potential energy surface* (cePES). To obtain them, we diagonalise the Hamiltonian of the confined coordinates at different points along the z axis; each z–dependent eigenvalue then conforms a given cePES.

In a previous work we proved that this adiabatic representation yields excellent agreement with full-dimensional propagations of the same system while drastically reducing the computational effort. For details on the derivation and the model of the 5D eigenstates, we refer the reader to Ref. 35.

Table 1. Primitive and SPF basis sets for the calculation of the eigenstates of the 5D Hamiltonian for both H_2 and D_2. Distances given in Bohr radii, angles in radians. The same primitive basis was used for both isotopologues.

DOF	Number of SPFs		Primitive grid		
	H_2	D_2	Num. Points	Type	Range
ρ	2	2	32	FFT	0.5–5.0
θ	5	5	64	cot-DVR	0–$\pi/2$
ϕ	7	7	64	FFT	0–2π
x	3	4	32	FFT	-3.5–3.5
y	3	4	32	FFT	-3.5–3.5

3. Results and discussion

3.1. Confined Eigenstates Potential Energy Surfaces

As a first step to study the diffusion, we took advantage of the adiabatic approach to visualise the diffusion process as a 1D problem. By observing the computed cePES we can obtain relevant information on the diffusion mechanism even before running actual quantum dynamics simulations of that process.

The SA-MCTDH approach was used to compute the eigenstates of the 5D Hamiltonian at the centre of a unit cell of the nanotube ($z = 0$) via iterative diagonalisation, using the same wave function representation parameters reported in [35] and listed in Table 1 for the sake of clarity. The 50 lowest energy eigenstates, $\xi_j^{5D}(q; z)$, were used as a basis for the matrix representation of $\hat{H}^{5D}$ at 512 equispaced points along the z coordinate, extending from -56.1 to 56.1 Bohr radii which corresponds to 14 unit cells of the SWCNT. The total number of carbon atoms used to define the interaction potential was large enough to ensure that no edge effects were noticeable at the ends of the simulation grid.

The lower energy cePES corresponding to the H_2 molecule are depicted in the left panel of Figure 2. The different curves are drawn according to the *ortho–para* symmetry of the 5D eigenstate they represent: the solid, darker lines label a symmetric state and the dashed, lighter lines label an antisymmetric state. The same scheme is followed in the right panel, which shows the curves for D_2. From these figures we can extract an approximate value for adsorption and for the threshold energy. The adsorption energy is given by the energy difference between the ground state of the free and the adsorbed molecule, and amounts to 0.36 eV for He and 0.30 eV for D_2. On the other hand, the threshold energy is is the minimum energy (including ZPE) that a particle would need to go from reactants to products. This quantity corresponds to the maximum of the lowest–energy cePES, and has a value of $E_{tr} = 0.3588$ eV for H_2, while for D_2 it decreases to $E_{tr} = 0.2543$ eV. The adiabatic diffusion barrier, ΔE_{tr}, defined as the difference between the maximum and the minimum of each cePES, is also slightly lower for D_2 (5.6 meV) than for H_2 (7.2 meV). A final feature is the density of confined eigenstates that each molecule presents. We can use the relation between flux eigenstates and the vibrational states of the transition complex to estimate how many eigenstates will contribute to the diffusion for a given energy range from the Boltzmann population of the vibrational levels of the molecule fixed at a point along the diffusion coordinate. It is readily seen that the spectrum is denser for D_2 than for H_2, as a consequence of its larger mass, and therefore more eigenstates will contribute to the diffusion for D_2 than for H_2.

All the effects presented in this section are directly or indirectly related to the differ-

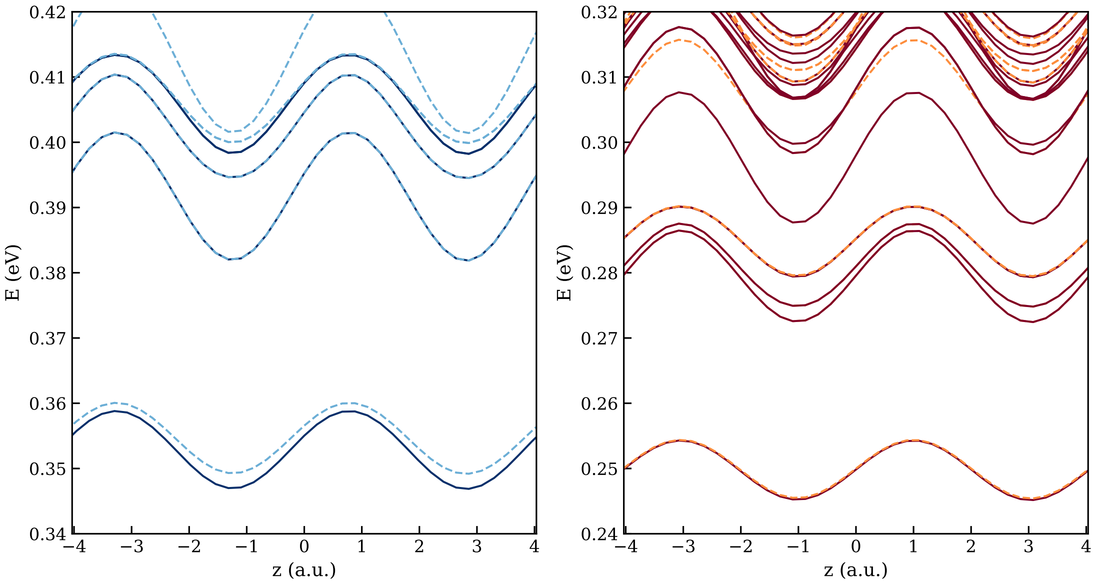

Figure 2. Variation along a single unit cell of the eigenenergies of the 5D hydrogen (left) and deuterium (right) eigenstates (cePES). Symmetric eigenstates with respect to inversion are represented with solid lines, while dashed lines label asymmetric states.

ent ZPE of the isotopologues, and point in the direction that, in confined environments, D_2 could diffuse faster than the lighter H_2. This *inverse kinetic isotope effect* has been described previously in Carbon Molecular Sieves[32, 34, 36, 51, 52] and nanotubes[37], and justified as a purely ZPE effect: due to the lower ZPE of D_2 its effective size is smaller than that of H_2, and as a consequence the heavier isotopologue feels less the corrugation of the potential generated by the Carbon atoms, thus diffusing more easily than H_2. In the next section, we will investigate if this effect persists when including all possible quantum effects via time–dependent quantum dynamics simulation of the system.

3.2. Hopping probabilities and diffusion coefficients

As outlined in Section 2.1, we used the flux correlation functions approach together with the SA-MCTDH method to compute the probability associated to the molecule transitioning between adjacent adsoprtion sites. Since quantum effects are more relevant at lower temperatures, we focus our study in the range of 40–125 K.

The qualitative analysis of the cePES above allowed us to estimate that only 6 to 8 flux eigenstates have an significant population at the maximum temperature considered, and therefore contribute appreciably to $k(T)$. To ensure convergence of the calculations we have computed a total of 26 flux eigenstates to represent the diffusion process of the H_2 molecule, and 30 in case of D_2. The basis set used to represent the MCTDH wave function in both cases is described in Table 2. Here it should be noted that since we are using a thermalised flux operator, it is necessary to choose an adequate thermalisation value β in order to get a numerically stable cumulative reaction probability. Values of β too high or too low will amplify the numerical noise

Table 2. Primitive and SPF representation used in the flux eigenstates calculation and propagation.

DOF	Number of SPFs		Primitive grid		
	H_2	D_2	Num. Points	Type	Range
q	20	14	50	Discrete	–
z	20	20	512	FFT	-56.066 – 56.066 a_0

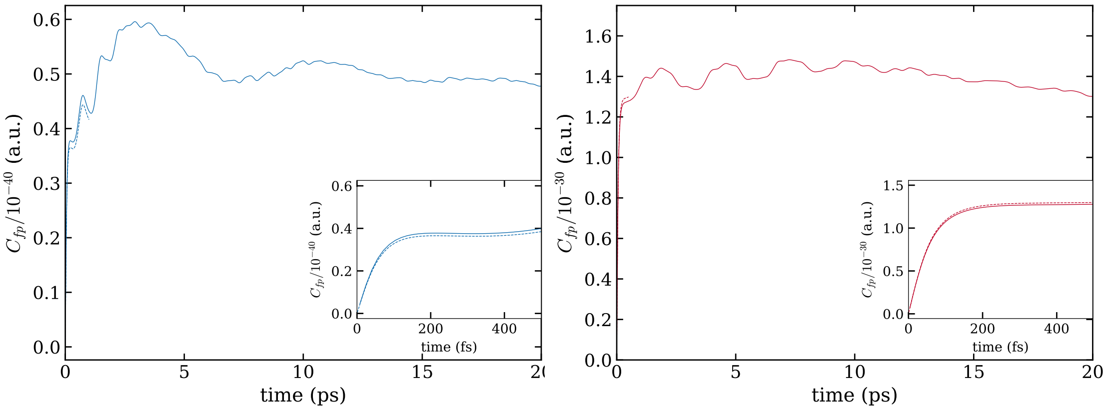

Figure 3. Flux–position correlation function for the diffusion of H_2 (right) and D_2 (left) along an (8,0) SWCNT. Inset: close up to the short–time region (dashed line corresponding to the 6D propagation in Ref. 37).

on the relevant energy region, thus yielding inaccurate results for $N(E)$ and ultimately for the diffusion coefficient. Here we set a value of β corresponding to 100 K, which was confirmed to yield numerically stable results in the investigated temperature range.

The resulting flux states were propagated for a total time of 20 ps, using again the SA-MCTDH method. To prevent transmissions and reflections in the edge of the representation grid we added a transmission–free complex absorbing potential (CAP) as defined by Manolopoulos[53, 54] with a length of 20 bohr. The transmission–free nature of the CAP was required due to the existence of long–lived processes in the diffusion mechanism (See below, and Ref.35, for details on these processes).

The integral of C_{ff} over time t, known as the *flux–position correlation function*, $C_{fp}(t)$, can be used as a rule of thumb to estimate the convergence of a calculation: the value of this quantity stabilises as the wave packet leaves the interaction region, and it reaches a plateau once the amplitude of the function in that region becomes zero. Therefore, to obtain a perfectly converged CRP one has to choose a propagation time t_f such that a constant value of $C_{fp}(t)$ is achieved for any time $t > t_f$. The flux–position correlation functions obtained after a total propagation time of 20 ps for H_2 and D_2 are shown in the left and right panel of Figure 3, respectively.

For the long time propagations reported in this work, note that in neither case does the function admittedly reach a constant value, thus indicating that a portion of the wave packets is still in the interaction region, even after 20 ps. This is a direct consequence of the small barrier for the diffusion process. Additionally, the fine structure of the functions is also a signal of the presence of resonances in the diffusion process[35]. These two features of the system would enforce us to go to much longer times to obtain a perfectly converged CRP. However, this time would only contribute to the resolution of the fine structure of the resonances, at the price of much more computational effort and potential numerical instability. Instead of this, we decided to fix the maximum energy resolution for the calculation of the CRP by multiplying

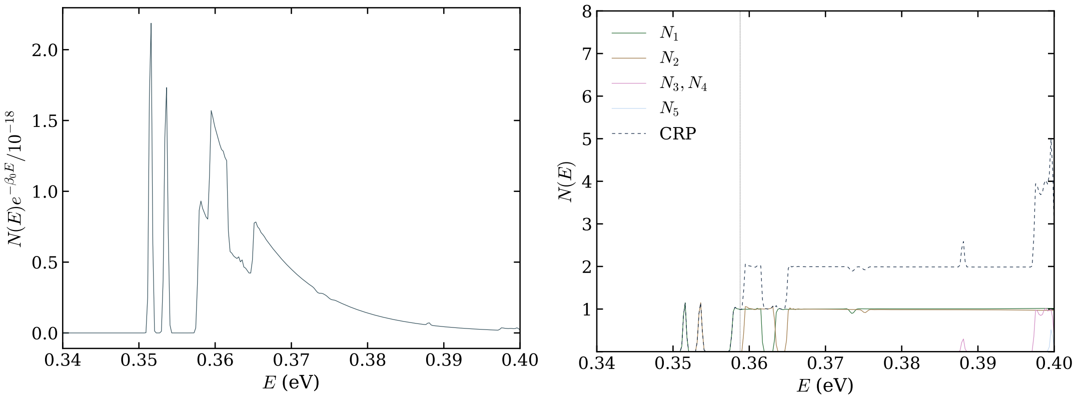

Figure 4. Cumulative Reaction Probability results for the diffusion of H_2. Left: Thermalized CRP at T = 100 K. Right: $N(E)$ and individual flux eigenstates contributions after 20 ps propagation. Vertical dotted lines marks the diffusion energy threshold.

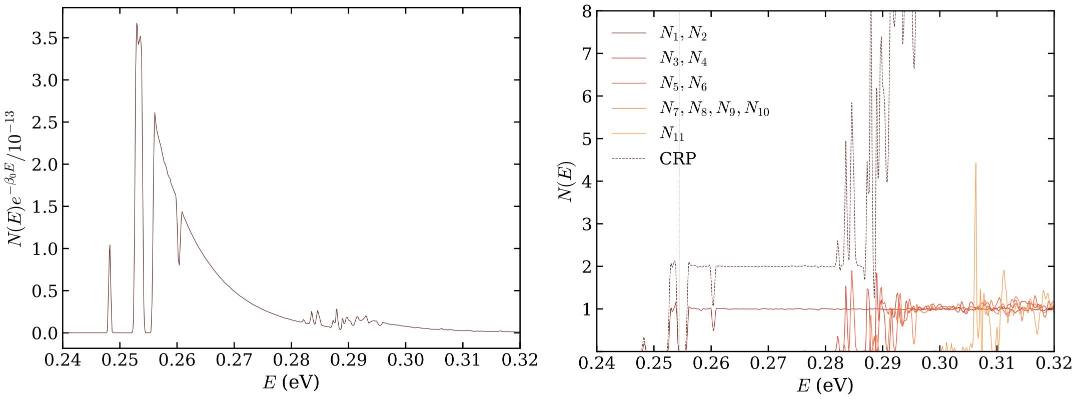

Figure 5. Cumulative Reaction Probability results for the diffusion of D_2. Left: Thermalized CRP at T = 100 K. Right: $N(E)$ and individual flux eigenstates contributions after 20 ps propagation. Vertical dotted lines marks the diffusion energy threshold.

$C_{ff}(t)$ by a Gaussian convolution function with $\Delta E = 0.12$ meV. This reduces the aliasing coming from the truncation of the Fourier Transform in Eq. 6[35], yielding a smoother function with better convergence properties and, as long as the value of ΔE is smaller than $k_B T$ for all the temperature range studied, not causing significant errors to the calculation of the transition rate, Eq. (2). To confirm that the CRP are sufficiently converged at 20 ps, we compared the resulting functions after an increase of 10% on the total propagation time, getting essentially the same results for both $N(E)$ and the transition rate.

The resulting $N(E)$ for H_2 and D_2 are shown in Figures 4 and 5, respectively, together with the individual contributions of the lowest–energy flux eigenstates. Additionally, the threshold energy for the diffusion process is marked in both figures as a dashed vertical line.

The first feature to notice in both plots is their significant amount of fine structure in form of sharp peaks. In a previous work[35] these features were confirmed to be shape and Feshbach resonances by calculating the exact 6D eigenstates of H_2 in a unit cell of the carbon nanotube using periodic boundary conditions and comparing its eigenvalues with the energies of the features on the CRP. In the mentioned work we were able to confirm the nature of these features: each peak on the CRP was related to two tunnelling eigenstates of the 6D system with opposite phase. The energy difference between these states corresponds to the width of the feature in $N(E)$ (see Ref. [35] for more details). The same kind of study for D_2 yielded similar results, thus showing that the features starting at 0.28 eV are indeed resonances and not numerical noise. By using the adiabatic picture of 1D wave packets in different cePESs and the concept of flux eigenstates as vibrational states of the transition state complex, we can get a qualitative interpretation of the resonances by assigning each flux eigenstate contribution (N_i in Figures 4 and 5) to a given cePES (for the lowest states, this can be easily done by comparing the energies of the features and the eigenstates). The sharp features then correspond to tunnelling-like states with an energy below the diffusion barrier for that specific cePES (shape resonances). For energies beyond this threshold the particle overcomes the potential barrier and diffuses freely, ($N_i(E) = 1$). On some particular states, there appear Feshbach resonances that slightly decrease this probability over a given energy interval (*e.g.* the two dips in aroung 37.5 eV of H_2). The large amount of resonant states is consistent with the shape of $C_{fp}(t)$ discussed previously, as the low-energy resonances provide a way for the wave packet to enter and leave the interaction region easily. More importantly, some resonances are found at energies below the diffusion threshold for both isotopologues, indicating that tunnelling effect is relevant for the diffusion process at low temperatures.

Comparing the cumulative reaction probability curves for both H_2 and D_2, one can see two main differences: on one hand, the energy and intensity of the first resonances; on the other, the density of the higher energy resonances. The first feature is probably the more critical point, since this difference will influence more heavily the behaviour of the different molecules at very low temperature. The two first resonances in $N(E)$ for the H_2 molecule are both intense and appear at energies significantly lower than the threshold. Moreover, a second-order resonance appears at $E = 0.36$ eV, just above the diffusion threshold, thus contributing to increase the diffusion coefficient at all temperatures. On the contrary, for D_2 we have a very weak (and therefore negligible) resonance at $E = 0.248$ eV, while two strong resonances exist at energies just below the energy threshold. However, since they are so close to the diffusion threshold, these resonances will have a smaller effect on D than those present in H_2. This can be understood by noticing that, in the calculation of the transition probability, Eq. (2), the CRP has to be weighted by a Boltzmann distribution and normalised with the partition function of the system. The latter avoids dependencies on the absolute energy scale chosen as reference, so that only relative differences in energy matter. Thus, as a result of the exponentially decaying Boltzmann function, the relative weight of the below-barrier resonances becomes larger in the overall diffusion probability as the temperature diminishes. As it can be seen in the left panel of Figures 4 and 5, where we show the CRP thermalized at 100 K, this effect becomes more noticeable as the energy difference between the tunnelling resonances and the diffusion barrier increases. In the case of H_2 diffusion, resonances are so apart in energy that, at very low temperature values, the two below-barrier resonances dominate the overall diffusion probability. Conversely, for deuterium the resonances are close enough to the barrier to contribute almost the same as the first above-barrier diffusion states at any given temperature value. This also explains why the effects of low–energy resonances decreases as temperature increases: as the above-barrier region gains weight due to the Boltzmann function, more diffusion states get populated, so the relative weight of the individual resonant states decreases. Similarly, even though D_2 presents a denser resonance spectrum than H_2 at high energies, these do not play any role in the diffusion process

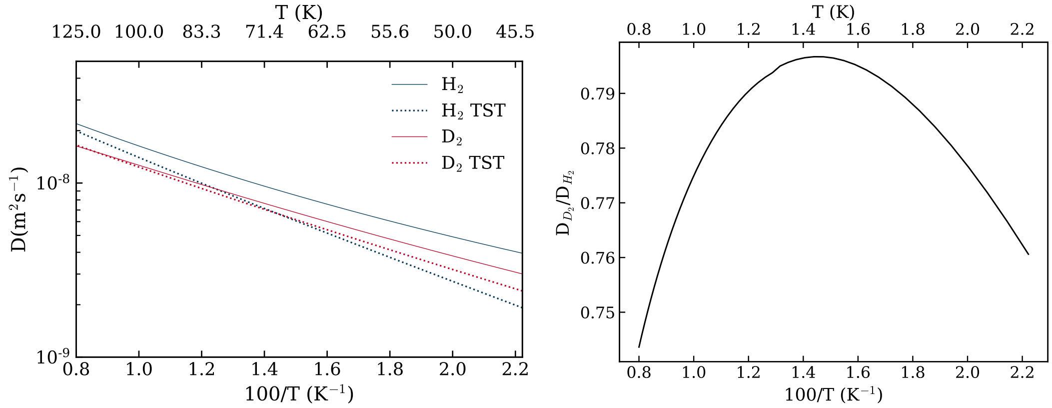

Figure 6. Left: Diffusion coefficient for H_2 (blue) and D_2 (red) computed with the flux correlation function approach (solid lines) and with TST (dotted lines). Right: Kinetic selectivity factor, defined as the quotient between the diffusion coefficients of D_2 and H_2.

in the studied temperature range, since the resonant states are too energetic to have significant population compared with the set of regular diffusion states.

Once we analysed $N(E)$ thoroughly, the transition coefficient has been obtained by Boltzmann averaging of the CRP at different temperatures, and then inserted in Eq (1) to compute the diffusion coefficient. The diffusion coefficient is plotted in Figure 6 as a function of temperature inverse for both H_2 and D_2 as solid blue and red lines, respectively. The same quantities have been computed using a Transition State Theory (TST) model, and are also shown in the same figure as dotted lines. The sum of all the quantum effects outlined previously (*i.e.* ZPE effects and tunnelling) significantly changes the diffusion coefficient with respect to those predicted by simple TST calculations. It is readily seen that there is a relevant increase of D at low temperatures for both isotopologues, but more so for the lighter H_2, as it was expected from the discussion of the cumulative reaction probability above. In fact, some tunnelling contributions remains at temperatures as high as 125 K for this molecule. The consequence of the different amount of tunnelling effect for both species is important even from a qualitative point of view: TST predicts a turnover of the diffusion coefficient at temperatures below 70 K, with D_2 starting to diffuse faster than H_2 at this point. This inverse Kinetic Isotope Effect is consistent with the discussion of the adiabatic diffusion barrier discussed Section 3.1 and widely studied in Carbon Molecular Sieves. In a previous work[37] we reported that the same effect would be observed for the diffusion of H_2 and D_2 along SWCNTs, and supported such a claim with quantum dynamics simulations of the full 6D system up to 500 fs. Instead, having been able to extend our quantum simulations to a remarkable limit such as 20 ps has changed dramatically our conclusions: 500 fs propagations provide insufficiently converged hopping probability, unable to resolve the sharp below tunnelling resonances. With the correctly converged cumulative reaction probability and the resonances properly resolved, tunnelling outweighs the ZPE effects at low temperatures, and the inverse kinetic isotope effect does not take place. As seen in the right panel of Figure 6, the kinetic selectivity, defined as the ratio D_{D_2}/D_{H_2}, presents a maximum of ≈ 0.8 around 70 K. This illustrates again the interplay between ZPE and tunnelling contributions: even though ZPE effects tend to increase D_2 diffusion, at $T < 70$ K they begin to be outweighted by the more efficient resonance enhanced diffusion of H_2. These results show the importance of an accurate quantum mechanical description of H_2 and D_2 when studying their diffusion properties.

4. Summary and Conclusions

The calculation of the diffusion coefficients for H_2 and D_2 along a (8,0) CNT in the low pressure limit has been carried out using the single–hopping approach. In this particular regime, intermolecular interactions are not expected to play a relevant role, both due to the low density of diffusing particles and the single-file diffusion imposed by the narrow cavity of the nanotube. Taking this into account, the hopping rate was obtained through the general expression of a transmission rate, with the cumulative reaction probability computed with the flux–correlation function approach. In order to achieve convergence of $N(E)$, we used an adiabatisation scheme to reduce the problem from a 6D Hamiltonian to a 2D system, thus being able to propagate the flux eigenstates for 20 ps. This allowed us to resolve resonant structures in $N(E)$ which enhance diffusion at low temperatures.

The diffusion coefficients calculated in this work differ from previous studies in that no inverse kinetic isotope effect appears in this particular system. This qualitative inconsistency with a previous work of us indicates that $N(E)$ was not correctly converged in those calculations. The difference with other theoretical and experimental studies on other nanostructured materials like Carbon Molecular Sieves, however, is probably due to the different structure of those, which present large pores connected through narrow channels rather than the cylindrical shape of carbon nanotubes. Despite this fundamental difference, and the use of the frozen nanostructure and low-pressure limits, we hope that this study about the behaviour of the molecules inside a carbon nanotube can be used to model the transport within the narrow channels connecting pores in other nanomaterials, or to consider the design of new devices based purely on nanotubes.

Acknowledgements

Financial support from the Spanish Ministerio de Economía y Competitividad (Ministry of Economy and Competitiveness) (CTQ2013-41307-P) and Generalitat de Catalunya (2014-SGR-25) is acknowledged. M.M.-M. further thanks a predoctoral grant from the FPU program (FPU2013/02210) from the Spanish Ministerio de Educación, Cultura y Deporte (Ministry of Education, Culture and Sports).

The Version of Record of this manuscript has been published and is available in *Molecular Physics* (22 June 2021) `https://doi.org/10.1080/00268976.2021.1942277`

Disclosure Statement

The authors declare no conflict of interest

Data Availability

The data that support the findings of this study are available from the corresponding author upon reasonable request.

Funding

This work was supported by the Spanish Ministerio de Economía y Competitividad (Ministry of Economy and Competitiveness) under Grant CTQ2013-41307-P and Generalitat de Catalunya under Grant 2014-SGR-25.

References

[1] S. Dunn, International Journal of Hydrogen Energy **27** (3), 235–264 (2002).
[2] L. Schlapbach and A. Züttel, Nature **414** (6861), 353–358 (2001).
[3] A.B. Basile, F.D. Dalena, J.T. Jianhua Tong and T.N.V. Vezirolu, editors, *Hydrogen Production, Separation and Purification for Energy* (, , 2017).
[4] I.V. Stiopkin, C. Weeraman, P.A. Pieniazek, F.Y. Shalhout, J.L. Skinner and A.V. Benderskii, Nature **474** (7350), 192–195 (2011).
[5] H.H. Mantsch, H. Saitô and I.C. Smith, Progress in Nuclear Magnetic Resonance Spectroscopy **11** (4), 211–272 (1977).
[6] J. Ewanicki, W. Kim and W. Wang, Magnetic Resonance in Chemistry **58** (8), 733–744 (2020).
[7] G. Büldt, H.U. Gally, A. Seelig, J. Seelig and G. Zaccai, Nature **271** (5641), 182–184 (1978).
[8] D. Liebschner, P.V. Afonine, N.W. Moriarty, P. Langan and P.D. Adams, Acta Crystallographica Section D: Structural Biology **74** (8), 800–813 (2018).
[9] About — Center for Gas Separations `http://www.cchem.berkeley.edu/co2efrc/about.html`, Accessed 28.03.2021.
[10] W.A. Van Hook, *Isotope Separation* (Springer US, Boston, MA, 2003), pp. 1863–1897.
[11] W. Spindel and T. Ishida, Journal of Chemical Education **68** (4), 312–318 (1991).
[12] H.K. Rae, in *Separation of Hydrogen Isotopes*, edited by Howard K. Rae, Vol. 10 (, , 1978), pp. 1–26.
[13] J.J.M. Beenakker, V.D. Borman and S.Y. Krylov, Physical Review Letters **72** (4), 514–517 (1994).
[14] Q. Wang, S. Challa, D. Sholl and J. Johnson, Physical Review Letters **82** (5), 956–959 (1999).
[15] T. Lu, E.E.M. Goldfield and S.S.K. Gray, Journal of Physical Chemistry B **110** (4), 1742–1751 (2006).
[16] G. Garberoglio, Chemical Physics Letters **467** (4-6), 270–275 (2009).
[17] P. Kowalczyk, A.P. Terzyk, P.A. Gauden, S. Furmaniak, K. Kaneko and T.F. Miller, The Journal of Physical Chemistry Letters **6** (17), 3367–3372 (2015).
[18] S. ullah Rather, International Journal of Hydrogen Energy **45** (7), 4653–4672 (2020).
[19] Y. Li and H. Liu, International Journal of Hydrogen Energy (2020).
[20] G. De Luca, Separation and Purification Technology **36** (3), 215–228 (2004).
[21] J.M. Salazar, M. Badawi, B. Radola, M. Macaud and J.M. Simon, Journal of Physical Chemistry C **123** (38), 23455–23463 (2019).
[22] B. Radola, M. Giraudet, I. Bezverkhyy, J.M. Simon, M. Salazar, M. Macaud and J.P. Bellat, Physical Chemistry Chemical Physics pp. 24561–2457 (2020).
[23] I. Bezverkhyy, M. Giraudet, C. Dirand, M. Macaud and J.P. Bellat, The Journal of Physical Chemistry C **124** (45), 24756–24764 (2020).

[24] H. Oh, M. Hirscher and H.I. Separation, European Journal of Inorganic Chemistry **2016** (27), 4278–4289 (2016).

[25] S.A. FitzGerald, K. Allen, P. Landerman, J. Hopkins, J. Matters, R. Myers and J.L. Rowsell, Physical Review B - Condensed Matter and Materials Physics **77** (22), 224301 (2008).

[26] J.Y. Kim, R. Balderas-Xicohténcatl, L. Zhang, S.G. Kang, M. Hirscher, H. Oh and H.R. Moon, Journal of the American Chemical Society **139** (42), 15135–15141 (2017).

[27] S.A. Fitzgerald, K. Shinbrough, K.H. Rigdon, J.L. Rowsell, M.T. Kapelewski, S.H. Pang, K.V. Lawler and P.M. Forster, Journal of Physical Chemistry C **122** (4), 1995–2001 (2018).

[28] D. Cao, J. Ren, Y. Gong, H. Huang, X. Fu, M. Chang, X. Chen, C. Xiao, D. Liu, Q. Yang, C. Zhong, S. Peng and Z. Zhang, Journal of Materials Chemistry A **8** (13), 6319–6327 (2020).

[29] T. Wang, E. Lin, Y.L. Peng, Y. Chen, P. Cheng and Z. Zhang, Coordination Chemistry Reviews **423**, 213485 (2020).

[30] J.Y. Kim, H. Oh and H.R. Moon, Advanced Materials **31** (20), 1805293 (2019).

[31] M. Liu, L. Zhang, M.A. Little, V. Kapil, M. Ceriotti, S. Yang, L. Ding, D.L. Holden, R. Balderas-Xicohténcatl, D. He, R. Clowes, S.Y. Chong, G. Schütz, L. Chen, M. Hirscher and A.I. Cooper, Science **366** (6465), 613–620 (2019).

[32] A.V.A. Kumar and S.K. Bhatia, Physical Review Letters **95** (24), 1–4 (2005).

[33] A.V.A. Kumar, H. Jobic and S.K. Bhatia, Journal of Physical Chemistry B **110** (33), 16666–71 (2006).

[34] A.V.A. Kumar and S.K. Bhatia, Journal of Physical Chemistry C **112** (30), 11421–11426 (2008).

[35] M. Mondelo-Martell, F. Huarte-Larrañaga and U. Manthe, Journal of Chemical Physics **147** (8), 084103 (2017).

[36] M. Hankel, H. Zhang, T.X. Nguyen, S.K. Bhatia, S.K. Gray and S.C. Smith, Physical Chemistry Chemical Physics **13** (17), 7834–44 (2011).

[37] M. Mondelo-Martell and F. Huarte-Larrañaga, Journal of Physical Chemistry A **120** (33), 6501–6512 (2016).

[38] D.H. Zhang, J.C. Light and S.Y.Y. Lee, Journal of Chemical Physics **111** (13), 5741–5753 (1999).

[39] J.D. Doll and A.F. Voter, Annual Review of Physical Chemistry **38** (1), 413–431 (1987).

[40] J. Barth, Surface Science Reports **40** (3-5), 75–149 (2000).

[41] T. Yamamoto, Journal of Chemical Physics **33** (1), 281 (1960).

[42] W.H. Miller, Journal of Chemical Physics **61** (5), 1823–1834 (1974).

[43] W.H. Miller, S.D. Schwartz and J.W. Tromp, Journal of Chemical Physics **79** (10), 4889–4898 (1983).

[44] F. Matzkies and U. Manthe, Journal of Chemical Physics **108** (12), 4828 (1998).

[45] U. Manthe, Journal of Chemical Physics **128** (6), 64108–12 (2008).

[46] T.J. Park and J.C. Light, The Journal of Chemical Physics **88** (8), 4897 (1988).

[47] U. Manthe and W.H. Miller, The Journal of Chemical Physics **99** (5), 3411 (1993).

[48] F. Huarte-Larrañaga and U. Manthe, Zeitschrift für Physikalische Chemie **221** (2), 171–213 (2007).

[49] M. Mondelo-Martell and F. Huarte-Larrañaga, Journal of Physics: Conference Series **635** (3), 032057 (2015).

[50] G. Garberoglio, M.M. DeKlavon and J.K. Johnson, Journal of Physical Chemistry B **110** (4), 1733–1741 (2006).

[51] T.X. Nguyen, H. Jobic and S.K. Bhatia, Physical Review Letters **105** (8), 085901 (2010).

[52] C.I. Contescu, H. Zhang, R.J. Olsen, E. Mamontov, J.R. Morris and N.C. Gallego, Physical Review Letters **110** (23), 236102–5 (2013).

[53] D.E. Manolopoulos, Journal of Chemical Physics **117** (21), 9552–9559 (2002).

[54] T. Gonzalez-Lezana, E.J. Rackham and D.E. Manolopoulos, Journal of Chemical Physics **120** (5), 2247–2254 (2004).